RESEARCH ARTICLE

NANO · MICRO small
www.small-journal.com

Stability of Ni–Fe-Layered Double Hydroxide Under Long-Term Operation in AEM Water Electrolysis

Irina Galkina, Alaa Y. Faid, Wulyu Jiang, Fabian Scheepers, Patrick Borowski, Svein Sunde, Meital Shviro, Werner Lehnert, and Anna K. Mechler*

Anion exchange membrane water electrolysis (AEMWE) is an attractive method for green hydrogen production. It allows the use of non-platinum group metal catalysts and can achieve performance comparable to proton exchange membrane water electrolyzers due to recent technological advances. While current systems already show high performances with available materials, research gaps remain in understanding electrode durability and degradation behavior. In this study, the performance and degradation tracking of a Ni_3Fe–LDH-based single-cell is implemented and investigated through the correlation of electrochemical data using chemical and physical characterization methods. A performance stability of 1000 h, with a degradation rate of 84 µV h^{-1} at 1 A cm^{-2} is achieved, presenting the Ni_3Fe—LDH-based cell as a stable and cost-attractive AEMWE system. The results show that the conductivity of the formed Ni-Fe-phase is one key to obtaining high electrolyzer performance and that, despite Fe leaching, change in anion-conducting binder compound, and morphological changes inside the catalyst bulk, the Ni_3Fe—LDH-based single-cells demonstrate high performance and durability. The work reveals the importance of longer stability tests and presents a holistic approach of electrochemical tracking and post-mortem analysis that offers a guideline for investigating electrode degradation behavior over extended measurement periods.

1. Introduction

The rapid growth in energy demand and the simultaneously increasing lack of fossil energy resources pose serious challenges to modern society.[1] As renewable power production has grown increasingly important in recent decades, green hydrogen production has become a promising large-scale technology for energy conversion, storage, and transport[2] with plans to reduce CO_2 emissions and other greenhouse gases worldwide.[3,4] Amongst the various methods of hydrogen production, water electrolysis is one of the most promising strategies for producing green hydrogen using renewable energy sources such as sunlight and wind.[5,6]

Industrial low-temperature (<100 °C) water electrolysis technology is governed by proton exchange membranes (PEMs) and alkaline water electrolyzers (AWEs). PEM water electrolyzers (PEMWEs) are highly efficient, but their harsh acidic reaction environment requires the use of

I. Galkina, W. Jiang, F. Scheepers, M. Shviro, W. Lehnert
Forschungszentrum Jülich GmbH
Institute of Energy and Climate Research
Electrochemical Process Engineering (IEK-14)
52425 Jülich, Germany
E-mail: ir.galkina@fz-juelich.de

A. Y. Faid, S. Sunde
Department of Materials Science and Engineering
Norwegian University of Science and Technology
Trondheim 7491, Norway

P. Borowski
Evonik Operations GmbH
45772 Marl, Germany

M. Shviro
Chemistry and Nanoscience Center
National Renewable Energy Laboratory (NREL)
Golden, CO 80401, USA

W. Lehnert
RWTH Aachen University
Faculty of Mechanical Engineering
Modeling in Electrochemical Process Engineering
52056 Aachen, Germany

A. K. Mechler
RWTH Aachen University
Electrochemical Reaction Engineering (AVT.ERT)
52056 Aachen, Germany

A. K. Mechler
Forschungszentrum Jülich GmbH
Institute of Energy and Climate Research
Fundamentals of Electrochemistry (IEK-9)
52425 Jülich, Germany

A. K. Mechler
JARA-ENERGY
52056 Aachen, Germany

The ORCID identification number(s) for the author(s) of this article can be found under https://doi.org/10.1002/smll.202311047

DOI: 10.1002/smll.202311047

expensive noble metal catalysts, that is, iridium and platinum, which are insoluble in acid in their oxidized states.[7] Traditional AWEs are operated with 25–40 wt% KOH and enable the use of non-noble metal components, such as low-cost steel or nickel alloy materials. Nonetheless, AWE systems employ thick diaphragms, which lead to low efficiency and performance due to the high Ohmic resistances that result.[8,9] The anion exchange membrane water electrolyzer (AEMWE) combines the advantages of high-performance PEMWEs, as well as traditional AWEs. As such, AEMWE allows the use of non-noble metals and low-cost materials due to operation in a non-corrosive environment. The use of a non-porous membrane allows a zero-gap design of the membrane electrode assembly (MEA), the advantages of which have been illustrated in previous studies of PEMWEs,[10] and so reduces the internal resistance and gas crossover. Moreover, the membrane-based assembly allows for asymmetric pressure operation of the cell,[11] thus facilitating the storage, distribution, and utilization of hydrogen.

Besides the intended increase in electrolyzer performance, decreasing the material costs is an essential aspect for the development and design of the electrodes. Replacement of the high-cost noble IrO_2 oxygen evolution reaction (OER) electrocatalyst would lead to the most significant potential for cost-reduction in the AEMWE system. Transition metal-based catalysts (Ni, Fe, Co) have drawn significant attention, as they provide excellent OER and hydrogen evolution reaction (HER) activities in alkaline media;[12-14] moreover, the use of earth-abundant and cheap materials is the easiest way to reduce the costs.[15-17] For instance, Fe is the fourth most common element in the Earth's crust, whereas Ni exhibits close to 100 ppm of abundance,[18] and therefore both are highly accessible elements for low-cost catalyst fabrication. This is one of the reasons why, amongst various non-noble metal-based OER catalysts, Ni–Fe-based electrocatalysts are still the most interesting and promising ones for AEMWE in alkaline media.[19,20] In particular, Ni–Fe-layered double hydroxides (LDH), with[21-27] or without doping elements,[28-34] have been intensively studied in recent years.[35] As OER catalysts, they exhibit very promising catalytic activity in alkaline environments.[36-39] Fe seems to stabilize the low-valent Ni centers, and so doping by Fe suppresses the oxidation of Ni^{2+} to $Ni^{3+/4+}$. The lower the average oxidation state of Ni, the faster the OER kinetics[40-42] and the more outstanding the catalytic activity for water-splitting.[26,43-45] The LDH structure, also called anionic or reffered as hydrotalcite-like clays, is comprised of layers of di- and trivalent metal cations centrally coordinated to OH^--anions and including guest anions such as CO_3^{2-}, intercalated between the layers.[46] They provide high oxidizing abilities and so even faster OER kinetics than basic Ni–Fe structures.

In the last few years, different configurations and types of NiFe-LDH-based catalysts have been studied in half- and single-cell set-ups, reaching performances of up to 1 A cm^{-2} at 1.67 V and stabilities of 50 h[47] and even 100 h at 1 A cm^{-2}.[48]

While much attention was focused on the development of active non-platinum group metal (non-PGM) catalysts[17,20,49–56] and stable and highly anion-conducting ionomers and AEMs,[57–64] the incorporation of non-PGM catalysts into a real single-cell testing including activity and long-term stability is still poorly studied in this research field.[59,65,66] The performance analysis of non-PGM catalysts is often limited by tests in rotating disk electrodes (RDEs) and to voltammetry cycling or several to tens of hours directly showing the first signs of degradation.[30,33,67] With respect to long-term stability tests of AEM systems, the operation time is usually limited to several hundred hours or even less.[22,23,51,68–70] Only a few long-term single-cell tests for AEMWE are described in the literature, presenting 500,[71] 1000,[72] or 2000 h[73,74] of operation; however, the chemical, electrochemical, and physical characterization of electrodes or MEAs are often missing although highly desirable.[70,75] The catalyst must be thoroughly analyzed before and after the single-cell measurements, using electrochemical and physical characterization methods[66] to understand real changes occurring as the catalyst is exposed to the actual electrolyzer environment. Although stability results from an RDE set-up do not necessarily unequivocally translate into stability in an MEA,[76] a post-mortem analysis is rarely presented, and we found a few reports on the post-mortem analysis of NiFe-LDH electrodes.

In this study, a promising Ni-enriched Ni_3Fe-LDH OER catalyst[54] was implemented in an AEMWE single-cell. Combined with the highly anion-conducting and stable membrane DURAION by Evonik and its corresponding preliminary anion-conducting binder, we offer a stable and low-cost MEA with high stability and efficiency. This study intends to present a general approach of single-cell durability tracking during long-term steady-state operation. In situ, electrochemical characterization is coupled with ex situ physicochemical methods to observe the internal chemical and morphological changes that occur on the anode–electrode. By this, we demonstrate a protocol of investigating and tracking the catalyst layer degradation in applied AEMWEs.

2. Results and Discussion

Figure 1A shows the single-cell that was employed, with the details explained in the Experimental Section (Supporting Information). For the anode fabrication, the Ni_3Fe-LDH electrocatalyst ink was directly deposited onto Ni fiber porous transport layers (PTLs) forming the anode–porous transport electrodes (aPTEs) as presented in Figure 1B. The Focused Ion Beam scanning electron microscopy (FIB SEM) cut catalyst-coated fiber reveals the properly enclosed PTL fibers (Figure 1C). The close-up cross-sectional SEM image of the coated fiber discloses the catalyst–binder distribution inside the catalyst layer, revealing bigger catalyst agglomerates of up to 2 µm and fine compounds of up to 50 nm. The final catalyst layer thickness varies from 5 to 15 µm relative to the spot observed, as seen in Figure 1C,D. A minor vertical crack formation and the homogenous particle distribution inside the catalyst layer were also confirmed by SEM and Energy dispersive X-ray analysis (EDX) mapping (Figure S1, Supporting Information).

2.1. Electrochemical Evaluation of NiFe LDH

As previously demonstrated by Jiang et al.,[54] the Ni-enriched Ni_3Fe-LDH shows higher electrocatalytic activity than the previously published NiFe-LDH catalysts with a differing Ni-to-Fe ratio. Thus, in this work Ni_3Fe-LDH, with an atomic ratio of Ni

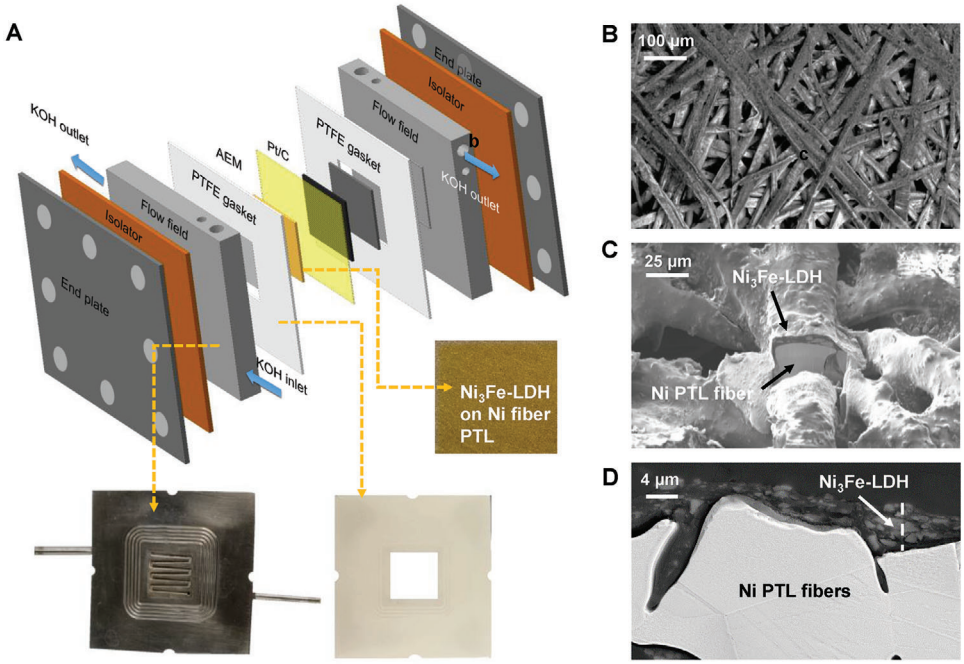

Figure 1. A) Schematic representation of the anion exchange water electrolyzer (single-cell) setup used in this study, including photographs of the aPTE, PTFE gasket, and flow field; SEM images of Ni_3Fe LDH coated on Ni fiber PTL: B) top-view; C) fib-SEM cut ofcoated Ni PTL fiber shown from a 45° angle; and D) cross-sectional image.

to Fe of 3:1, was selected as the OER catalyst for implementation into the AEMWE system. Before investigating the single-cell performance, Ni_3Fe-LDH was compared to Ir, as Ir or IrO_2 are considered anode baseline materials for PEMWE[10,77] and AEMWE.[17,59,78–82] All test parameters and conditions are described in the Experimental Section (Supporting Information). The successful deposition of both catalysts on the Ni–PTL was proved by X-ray diffraction (XRD), for which characteristic peaks for Ir (Figure S2A, Supporting Information) and Ni_3Fe-LDH according to the respective powder pattern (Figure S2B, Supporting Information) were found. SEM analysis of the aPTEs and cross-sections thereof showed a full coverage of the Ni–PTL fibers, as well as similar catalyst layer thicknesses for both the Ir and Ni_3Fe-LDH of ≈6–10 µm at loadings of 1 mg cm^{-2} (Figure S3, Supporting Information). Both aPTEs were evaluated for their performance under equal conditions, as described in the Experimental Section (Supporting Information). Higher currents were achieved at the Ni_3Fe-LDH aPTE over the entire potential range, with a maximum current density of 2 A cm^{-2} at 2 V more than the Ir cell, which only reached 1.3 A cm^{-2} at 2 V (Figure S4A, Supporting Information). The better Ni_3Fe-LDH cell performance is explained by the higher catalytic mass activity of the Ni_3Fe-LDH OER catalyst in comparison to Ir (or IrO_2), as already reported in the literature.[19,30,54] Furthermore, a better contact of the Ni_3Fe-LDH catalyst on the PTL was visible from the EIS analysis, where the charge transfer resistance (R_{ct}) of the Ni_3Fe-LDH aPTE achieved 184 mΩ cm^2 with respect to 218 mΩ cm^2 for the Ir-based aPTE (Figure S4B, Supporting Information).

The Ni_3Fe-LDH single-cell performance with a higher catalyst loading of 2 mg cm^{-2} on the aPTE is presented in **Figure 2A** reaching 1 A cm^{-2} at 1.77 V or 2 A cm^{-2} at 1.97 V. Following iR-correction, only 1.69 V were needed to achieve 1 A cm^{-2}. For this study, a loading of 2 mg cm^{-2} of Ni_3Fe-LDH was chosen to enable post-mortem analysis of the catalyst layer. This catalyst loading was comparable to other reported loadings for non-PGM catalysts.[69,83–85] The loading range is said to be cost-effective, but is still high enough to reach high single-cell performance and durability. Furthermore, the presented Ni_3Fe-LDH–Pt/C single-cell performance is comparable or higher than the results already presented the in literature.[25,30,86,87] It should also be noted that all of the used materials and parameters can influence the performance values. For instance, the use of carbon felts as PTL has been reported to increase AEMWE performance.[25]

To track steady-state long-term stability, the cell was subjected to a constant current density of 1 A cm^{-2} for 1000 h, with performance and EIS measurements every 100 h. Figure 2B shows the resulting potential across the entire durability test, as well as the calculated cell voltage efficiency (Equation S1.1, Supporting Information).[30] During the first 200 h, a decrease in cell potential by ca. 39 mV was observed. This most likely corresponds to a break-in of the cell where the optimal interface between the catalyst and electrolyte is formed.[88] This behavior differs from the one reported in the literature for NiFe-LDH-based electrolyzers,[25,30,31,33] where a recently reported break-in procedure lasts for ≈80 h.[71] Still, decreasing voltage behavior is not uncommon and often presented in literature;[49,71,72] it is to be expected that ion exchange and soaking of the membrane still proceeds to some degree. Moreover, the catalyst is oxidized to active species layer by layer as the Ni_3Fe-LDH catalyst used here is a multilayered catalyst. In addition, the catalyst agglomerate size inhomogeneity, that is, in the range of 1–100 µm, which is an important parameter of the catalyst layer formed in this work

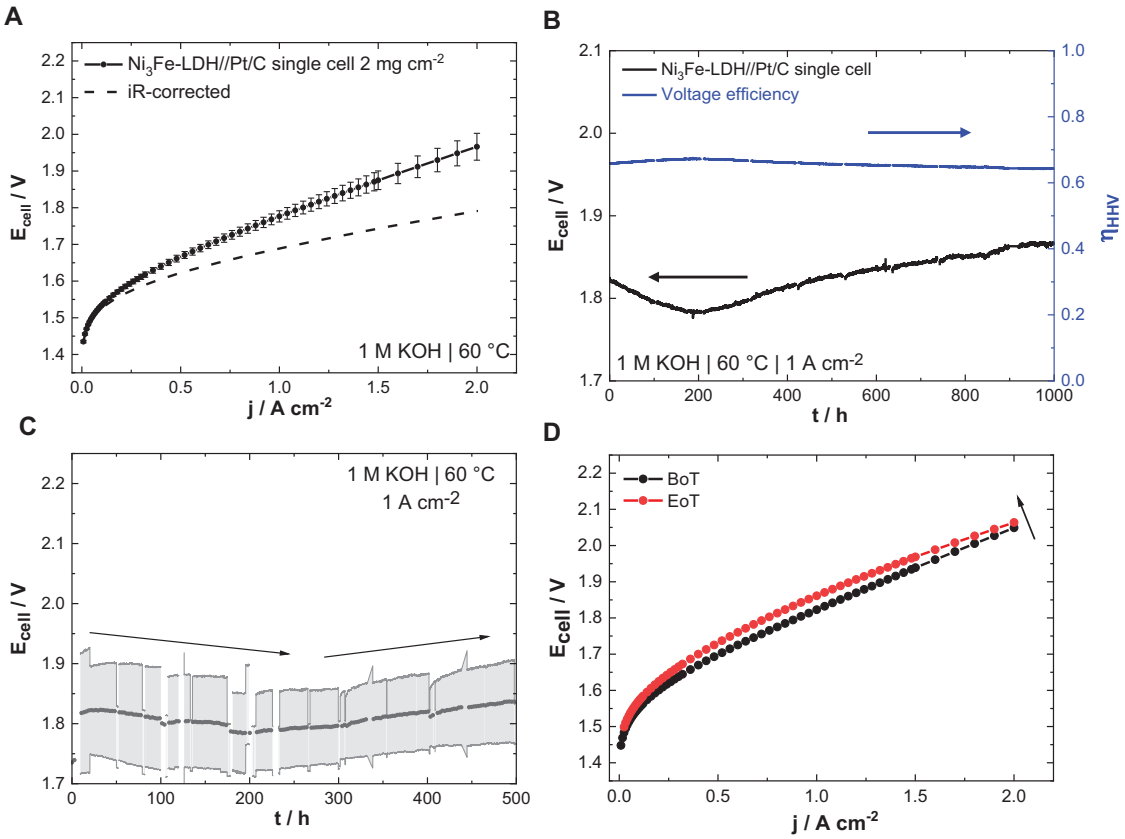

Figure 2. A) Polarization curve of the Ni_3Fe-LDH cell system, incl. iR-corrected UI-curve; B) cell voltage and voltage efficiency during long-term 1000 h single-cell operation at a constant 1 A cm^{-2} in 1 M KOH and 60 °C; C) time-resolved cell voltage change incl. reproducibility measurements; D) polarization curves at beginning of test (BoT) and end of test (EoT, after 1000 h).

and that is supposed to be the main factor in the long conditioning procedure. Furthermore, following the observed conditioning of 200 h, where the oxidation of Ni_3Fe-LDH to the active γ-NiOOH occurs, additional Fe is absorbed from the electrolyte. Combined with the existing amount, this creates an increase in the Fe content that is sufficient to significantly increase the catalytic activity.[38]

The determination of the moment at which the system is considered to obviously start degrading is a topic for deeper discussion, as the system break-in (conditioning) time should be carefully investigated and defined for each AEMWE system. Different types of cell voltage behaviors have been observed during the long-term tests described in the literature.[88] As different processes inside a cell can occur simultaneously and overlap, the reported rate of cell degradation may not provide a true representation of the cell's actual degradation process. The terms degradation, durability, and stability are used in literature for the description of different voltage trends.[49,68,71,72,89,90] Those include the decrease, increase or even a mixed behavior in which one type follows the other. In this study, we differentiate between the overall voltage increase (end of test (EoT) minus beginning of test (BoT) values (or EoT–BoT)) and degradation, in which the voltage values are considered from the lowest value (200 h) to the highest and final voltage at EoT. Following this terminology, the cell presents a low overall voltage increase of 45 μV h^{-1} (2.49%) and a considered cell degradation from 200 h of 84 μV h^{-1} or 4.68%. This is significantly lower than previously reported for NiFe-LDH catalysts.[25,91] Interestingly, the cell voltage efficiency is only marginally affected by the potential change. Over the course of the entire experiment, it is in the range of 64–65%, which is comparable to previously reported values.[30]

After the long-term operation, a color change in the aPTE was observed (Figure S5A, Supporting Information). The transformation from yellow–orange to brown–black indicates an oxidation of the catalyst layer. The membrane, however, did not show a color change and was not visibly damaged after the long-term test. Some residues of the applied pressure inside the cell, as well as minor catalyst leftovers from both sides, are also visible (Figure S5B, Supporting Information).

The long-term stability was further repeated three times with a shorter operational duration of 500 h (**Figure 3C**) to investigate the reproducibility of the degradation trends. A scattering of performance of ≈200 mV at 1 A cm^{-2} was obtained due to the use of different material batches, whereas the trend of ≈200 h break-in time is reproducible.

To identify possible sources of the performance lost during steady state single-cell operation, the intermittent polarization curves and EIS data were analyzed. Figure 3D presents the polarization curves at the BoT and EoT. At 2 A cm^{-2} the potential increases by ca. 15 mV, which is only a minor increase in cell

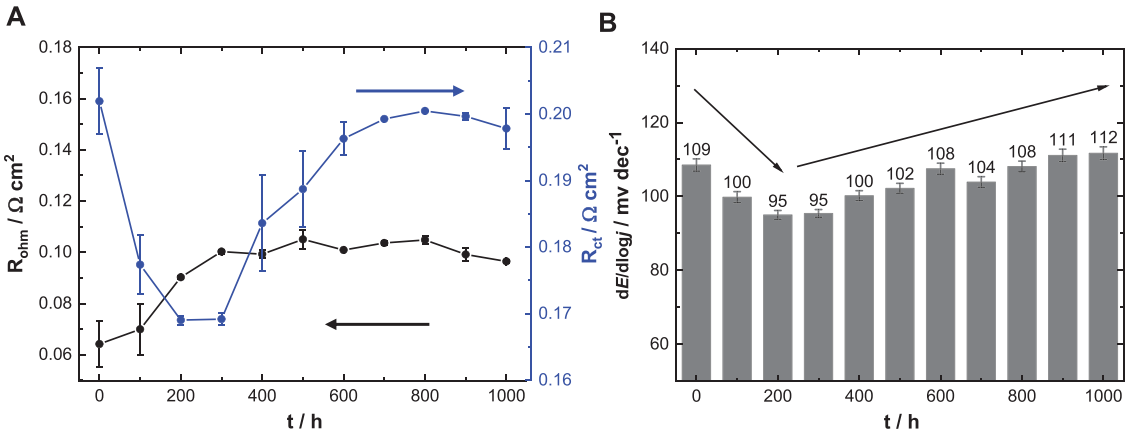

Figure 3. Ni_3Fe-LDH cell: A) Time-dependent change in R_{ct} and R_{Ohm} of the system obtained from in situ impedance spectroscopy analysis; B) time-dependent change of the $dE/d\log j$ slopes.

voltage. Figure S6A (Supporting Information), furthermore, shows the significant performance gain during the first 200 h of operation, with a maximum performance of 1.96 V at 2 A cm^{-2} and a decrease of R_{ct} down to 0.168 Ω cm^2 (Figure S6B; Table S1, Supporting Information).

Figure 3 shows the time-resolved trends of R_{ohm} and R_{ct}. As the Nyquist plots do not intersect the x-axis (Figure S6B, Supporting Information) and the plot fit is extrapolated, there is a variation in the simulated high-frequency resistance values (R_{ohm}). To ensure the reproducibility of the obtained values, the fitting procedure was repeated three times (Table S1, Supporting Information). During the stability test, R_{ohm} increased from the BoT to EoT by 32 ± 1 mΩ cm^2 (Figure 3A, black curve). A significant portion, that is, 26 ± 1 mΩ cm^2, was observed during the first 200 h of operation. This increase might indicate a minor initial change in the membrane or anion-conducting binder in the catalyst layer, or a change in the interface membrane–electrode, which stands, at first glance, in contrast to the overall performance observed during the break-in time. Furthermore, no major change in the R_{ohm} value was detected for the rest of the test. The R_{ct} values, reflecting the charge–transfer resistances of both OER and HER, $R_{ct,a}$, and $R_{ct,c}$, respectively, exhibit a more complex trend (Figure 3A, blue curve). First, up to 200 h, a decrease is noticeable, indicating improved charge transfer kinetics. This is in line with the increase in OER performance during this period and could have a stronger influence than the increase in R_{ohm}. Furthermore, the observed increase in the R_{ct} after 300 h correlates well with the degradation of the cell as observed in the potential trend (Figure 2B). The increase in R_{ct} could be related to a partial loss in electrocatalytic activity and a decrease in the electrochemical surface area by losing or deactivating catalyst and/or binder material; precise deconvolution of the effects is not trivial without extended studies of the anion-conducting binder compound.

The change in catalyst kinetics is further confirmed by changes in the actually observed current increase rate. By that, the change in the slope of the potential (iR-corrected) versus logarithm of current densities j is meant ($dE/d\log j$) (Figure 3B). The $dE/d\log j$ slopes were extracted from a linear fit of the polarization curves on a logarithmic current scale, following iR correction, in the current density range of 0.03–0.1 A cm^{-2} (Figure S7, Supporting Information). This narrow region was chosen to account for primarily kinetic effects, avoiding the possible effects of the saturation of surface coverage of adsorbates and mass transport limitations. Starting with 109 ± 2 mV dec^{-1}, the $dE/d\log j$ slope slightly decreased for the first 300 h of operation to 95 ± 1 mV dec^{-1} and subsequently increased to 112 ± 2 mV dec^{-1}. These observations correlate well with the trend of charge–transfer resistances (Figure 3A) and the overall durability trend (Figure 2B), fitting the correlation between those parameters. The $dE/d\log j$ slope is inversely proportional to the charge–transfer coefficient and therefore proportional to the charge–transfer resistance. Contributions from changes in cathode performance and partial cover effects may be non-negligible, as the current–voltage trend contains both of the electrodes. A separation of the overlapping contributions is, however, not trivial.[92] As the OER is slower and considered the more energy-demanding reaction,[49,93] it is expected that the contribution of the anode, the Ni_3Fe-LDH aPTE in this case, will be more pronounced.

After 1000 h of operation, the single-cell was disassembled and the original electrodes were re-assembled with a fresh membrane. Interestingly, performance regeneration was observed that almost reached the performance obtained after 200 h, which was achieved shortly after the break-in time (Figure S6A, Supporting Information). This also corresponded to a reset of R_{ct} as well as a decrease in the Ohmic resistance (R_{ohm}) (Figure S6B; Table S1, Supporting Information). During the AEM exchange procedure, in addition to a refreshment of the membrane, the re-assembly could lead to improved contact between the electrodes and membrane. Furthermore, the re-assembly of the cell could induce further effects like bubble removable. Whether the different effects of the replacement of the membrane or restart have a greater influence, and to what extent, remains unclear from this study and should be further investigated in future.

Previously, the lack of stability of layered double hydroxides was considered to be a challenge for industrial-scale application.[66,94] Due to results obtained on the laboratory scale, the LDH catalysts are still discussed as being insufficiently stable for the real electrolyzer environment.[70] Typically, the durability of AEMWEs is poor and typically discussed after

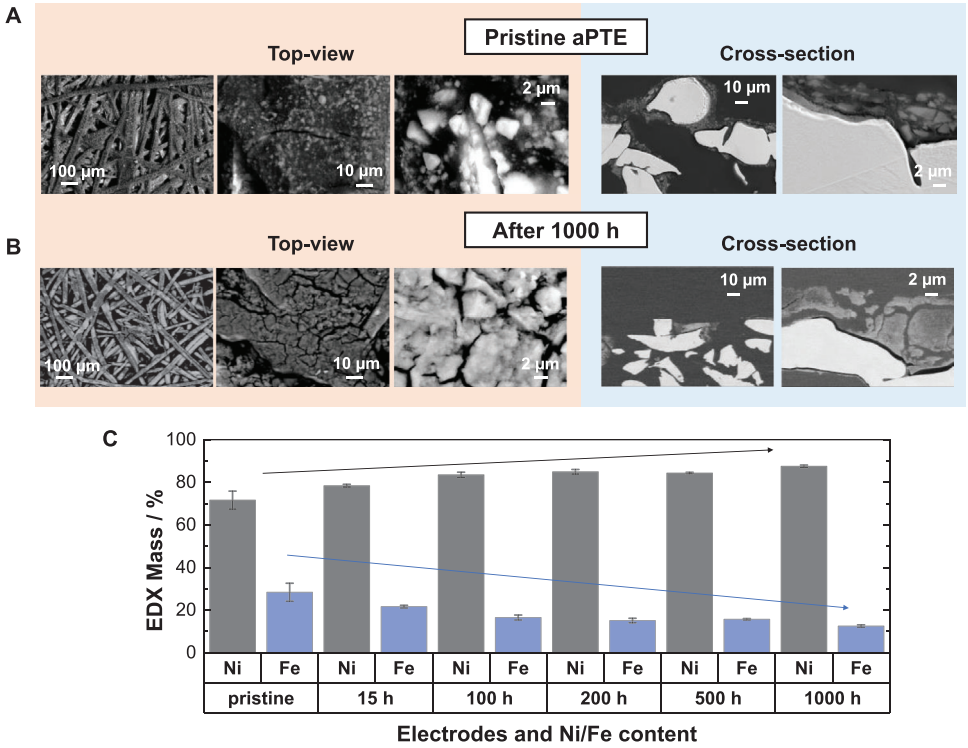

Figure 4. Top-view and cross-section SEM images at different magnifications of A) pristine Ni_3Fe-LDH aPTE, B) aPTE after 1000 h of operation; C) EDX analysis results of the aPTEs for Ni and Fe from a pristine sample to a 1000 h one (cross-sections of catalyst bulk analyzed).

relatively short-term periods of operation of ≈100 h and/or in less rigorous conditions like low current densities and operating temperatures.[16,24,30,33,67] The supports used (PTLs) are often carbon-based and display a high tendency toward oxidation and degradation,[95–98] or high loadings[96,98,99] of the catalysts are used. The post-mortem analysis of the structure and morphology of electrodes is often missing, raising doubt as to the real non-PGM-based electrode stability.

With our electrochemical characterization under applied conditions, we show a Ni_3Fe-LDH-based MEA that demonstrated stable operation in a single-cell for 1000 h. This is outstanding compared to typical values. In addition, far too little attention in is paid in the literature to the reproducibility of long-term tests due to the time required for single-cell measurements and the uncertainty of system behavior. Most literature in the PEM and AEM research fields focuses on the degradation behavior presented by only one time-resolved curve[88,100–103] or rounds of voltammetry cycling operation.[104] Here, the reproducible voltage trend of 500 h, including a break-in behavior of ≈200 h, was proved by a repetition of the long-term tests. To better understand the induced changes brought about by the long-term electrochemical operation, further analytical techniques were applied post-operando.

2.2. Morphological and Elemental Degradation Studies on the aPTE

Figure 4A presents the top-view and cross-sectional scanning electron microscopy (SEM) images of the Ni_3Fe-LDH aPTE directly after fabrication, whereas the same electrode after 1000 h of operation is shown in Figure 4B. The intermediate conditions of the aPTE after 15, 100, 200, and 500 h are presented in the (Figure S8, Supporting Information). It should be noted that due to the necessity of disassembling the cell, each figure set corresponds to a new electrode and experiment.

The pristine aPTE (Figure 4A) exhibits proper coverage of the Ni PTL fibers. Due to the relatively low catalyst loading of 2 mg cm^{-2}, the resulting catalyst layer is distributed over the individual fibers rather than forming a closed layer — a phenomenon observed with higher catalyst loadings and thus increased layer thickness. The initial catalyst layer demonstrates minor fractures, likely induced by the drying process and flexibility of the PTLs. The cross-sectional images reveal the binder–catalyst distribution, the catalyst agglomerate size, and the catalyst layer thickness. After 1000 h of operation, a partial catalyst layer delamination becomes evident.

When discussing the changes in the catalyst layer, the damage that occurred when the MEA was disassembled from the cell hardware should be considered (Figure S9, Supporting Information). In particular, some parts of the catalyst layer remained attached to the membrane. The use of an aPTE with higher loading (for example, 5 mg cm^{-2}, as presented in Figure S10A,B, Supporting Information) would lead to negligible changes, revealing the actual stable catalyst layer and thus electrode structure.

Comparing the top-view images of the pristine aPTE and the one after 1000 h (Figure 4A and B), a roughening of the catalyst layer surface can be observed. Moreover, the crack formation becomes more pronounced. The cracks do not necessarily lead to a loss of activity, as long as the amount of attached catalyst does not

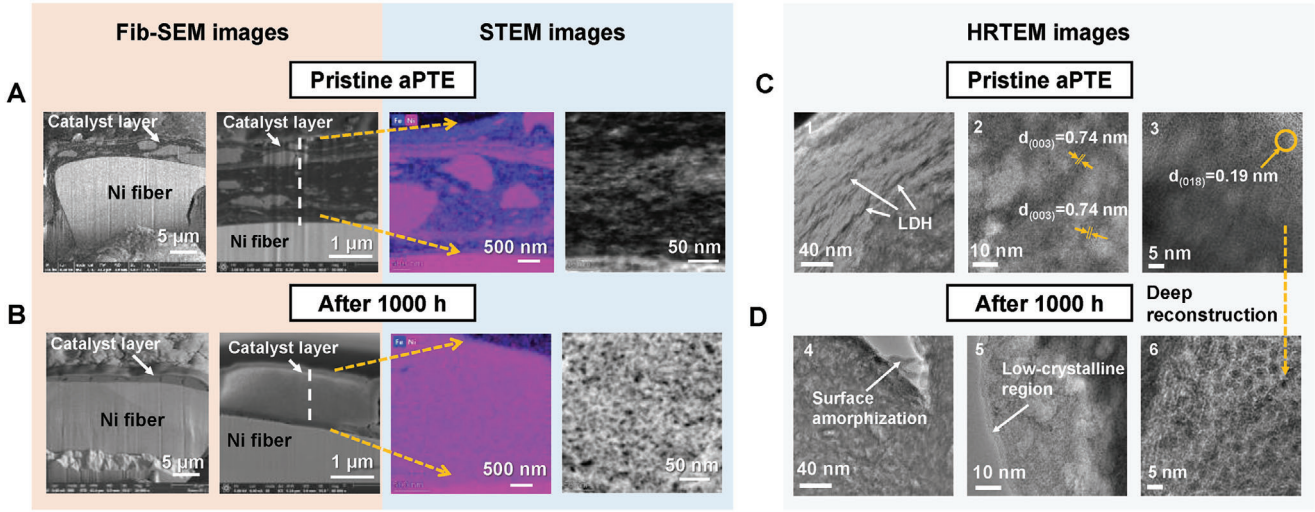

Figure 5. SEM images of fib-cut Ni PTL fibers coated with catalyst layers and STEM images of the catalyst layer, incl. EDX-mapping for Ni and Fe: A) for initial (pristine) aPTE; and B) after 1000 h; HR-TEM images of C) initial (pristine) catalyst layer of aPTE (1–3); D) catalyst layer after 1000 h of operation (4–6) with different magnifications.

drastically diminish and the different parts remain in electrical contact, as well as being well attached to the membrane. It was already proven that a cracked surface might even be preferred, as it helps with faster bubble removal and might even decrease catalyst dissolution during OER.[105]

The apparent roughness of the catalyst layer can also be explained by the ablation of the catalyst layer or the relative reduction in the binder compound content[106–109] that appeared during the single-cell test, as was also shown by time-of-flight secondary ion mass spectrometry (TOF-SIMS) analysis below. This could also explain the increase in R_{Ohm} over the course of the experiment, as the contact between the catalyst and binder, and respectively the membrane, is decreased. Nevertheless, even after 1000 h, the overall catalyst layer mostly appears to be stable. Neither thinning of the layer nor full delamination from the PTL substrate can be recognized.

Interestingly, the cross-sectional images reveal a significant structural change in the catalyst particles after 1000 h. A slight re-dispersion within the catalyst layer can already be seen after 500 h. A more detailed examination of the changes within the catalyst layer bulk is outlined in the next section. The reconstruction of the catalyst layer is often considered one of the main causes of degradation. Another critical degradation factor is the leaching of chemical elements, that is, Fe in NiFe-based catalysts.[70] Therefore, we analyzed the metal contents of the extracted aPTEs by means of EDX. Figure 4C presents the mass percentage of Ni and Fe contained in the catalyst layer bulk of the aPTE after different stages of the durability test (0, 15, 100, 200, 500, and 1000 h). Based on the initial aPTE with a mass ratio of (3 ± 0.4):1 Ni:Fe, the Fe content is continuously decreasing and reaches a final ratio of (7 ± 0.3):1 after 1000 h, confirming the leaching of Fe and an enrichment of Ni. This is confirmed by the analysis of the electrolyte after 1000 h of operation by ICP–MS (Table S2, Supporting Information). Although the pristine electrolyte already contains Fe (50–90 µg L^{-1}), Ni (10–70 µg L^{-1}) and other trace elements (<1 µg L^{-1}), the Fe content increased dramatically at EoT to 200–400 µg L^{-1}, whereas the Ni content decreased (<3 µg L^{-1}). Fe leaching is extensively discussed in the literature, but the mechanisms are not yet fully understood. For instance, under electrochemical conditions, anodic polarization leads to oxidation of the metal sites within the Ni_3Fe-LDH. It is expected that this can lead to structural or composition changes.[110] Thus, we also assume a restructuring of the catalyst due to Fe loss. Although Fe has been discussed in the literature as the active site for OER,[42,44,111,112] for example, due to the short Fe—O bond;[42,112] in our work, the single-cell performance remains at a high level, even after long-term operation and in spite of the significant Fe leaching. Furthermore, in the literature it has been reported that the actual content and means of preparation or incorporation of the Fe^{3+} compound does not play a significant role.[42] Thus, even the low amount of Fe remaining in the catalyst structure could be sufficient for promoting the high activities recorded.

The catalyst layer composition was further investigated using highly-resolved SEM and scanning transmission electron microscopy (STEM) analyses. The images were made on a 250 µm Focused Ion Beam (FIB) lamella cut from a catalyst-coated Ni fiber. **Figure** 5A shows the cross-section of a single catalyst-coated Ni PTL fiber of the initial aPTE at different magnifications. The initial catalyst layer presents lighter and darker areas, in which the lighter ones are assigned to the catalyst particles with a homogeneous distribution of Ni and Fe and the darker areas are the anion-conducting binder mixed with smaller catalyst particles. The initial aPTE exhibits irregular catalyst particle sizes with agglomerates up to 1 µm, which are supported by the EDX mapping results. The agglomerates confirm both Ni and Fe elements with a ratio of 3:1. After 1000 h (Figure 5B), a sponge-like structure of the catalyst layer is recognized, which is reported for structures converting to oxyhydroxides.[70,113] Various non-PGM catalysts, especially Ni–Fe-based ones, are known for structural evolution under electrochemical conditions.[112,114] The Ni_3Fe-LDH morphological changes can be related to the influence of the

surface tension of oxygen evolution bubbles that can squeeze ultrathin and flexible LDH nanosheets and significantly alter the Ni_3Fe-LDH surface morphology.[67,115] Likewise, CoO, which is electrochemically-oxidized in alkaline media, is known to undergo a considerable morphology change by breaking bigger material particles into many interconnected smaller grains under In situ electrochemical oxidation. This phenomenon fosters a well-distributed layer of small catalyst particles, creating numerous nanopores.[116] In the present case, Ni and Fe are well-distributed amongst the homogenized catalyst layer and no other agglomerates are visible. Significant film rupture was, moreover, not observed.

Ex situ high-resolution transmission electron microscopy (HR–TEM) was carried out on the initial sample (Figure 5C1–3), as well as after 1000 h of operation (Figure 5D4–6) to further investigate the morphological evolution of the Ni_3Fe-LDH electrodes. To confirm the initial Ni_3Fe-LDH's existence and its structure on the pristine aPTE, the lattice fractions of several areas were analyzed. The darker areas of image 1 can be attributed to the stacked LDH nano-sheets, which were previously presented in the literature.[31,54,117,118] Images 2 and 3 show the higher magnified HR–TEM images, in which the basal spacing along the c-axis of 0.74 nm and the distance of 0.19 nm are measured, corresponding to the (003) and (018) planes (Figure S11, Supporting Information).[36,119,120] The calculation of lattice fractions for the sample after 1000 h is not meaningful, as those of Ni_3Fe-LDH, NiOOH and FeOOH can be recognized, whereas the values of the measured distances are too close to be clearly identified. The LDH nano-sheets are still partially visible after 1000 h (image 4), as the NiFe-LDH formation is reversible. The long-term operation does not harm the nano-sheets. The HR–TEM images (image 6) exhibit a mosaic texture with domains up to 5 nm with a large concentration of micro-strains, even more than in the initial sample. This appearance was previously reported for β-NiOOH.[121] Although the structure of the formed oxides and oxyhydroxides was claimed to be amorphous, it can be assumed that the 1000 h of aPTE presents a mixed structure of NiFe-LDH and the Ni- and Fe-hydroxides. Local crystallite spots are visible, whereas the outer parts of the catalyst layer after 1000 h exhibit amorphilization (images 4 and 5).

Overall, in our study an LDH structure collapse was not confirmed, while elemental leaching indeed took place during single-cell operation, as confirmed by EDX on the aPTE cross-sections and the ICP–MS analysis of the electrolyte previously. In addition, a significant catalyst layer reconstruction took place without affecting the single-cell's overall performance.

Typically, these findings are made at the laboratory scale in a three-electrode cell setup, which is a poor system to be compared with a real-world single-cell. In our case, interestingly, the implementation of the NiFe-LDH and leaching behavior was consistent with the one conducted in the laboratory of the three-electrode set-up.

In order to prevent the observed morphological changes, we propose operating electrolyzers with Ni_3Fe-LDH and potentially also other Ni–Fe-LDHs electrodes at lower potentials, and to control the lowest and highest cut-off voltages. Furthermore, the use of a Fe-enriched electrolyte may prevent or slow down this degradation mechanism.

2.3. Atomic and Electronic Structure Investigation of the aPTE

For the LDH catalysts, the structure collapse, especially upon thermal treatment,[122,123] morphological reconstructions,[67] and active component leaching are the main stability issues.[70] To understand the chemical and physical changes during 1000 h of single-cell operation, several analysis methods were conducted ex situ on the aPTE. As already mentioned previously, the initial aPTE has an inhomogeneity of the catalyst phase and particle size and local catalyst/binder inhomogeneity, which has an influence on the X-ray photoemission spectroscopy (XPS) and XRD data.

Figure 6A displays the XRD patterns of the Ni_3Fe-LDH aPTE directly following the fabrication process (pristine) and 1000 h of single-cell operation. The intermediate states after 100, 200 and 500 h of operation are presented in Figure S12 (Supporting Information). The initial XRD spectra provides all expected peaks for the NiFe-LDH (JCPDS#40-02 15 NiFe-LDH).[32,124,125] The XRD patterns of all samples display peaks at 2Θ values of ≈12°, 23°, 35°, and 60°, corresponding to (003), (006), (012), and (110) of Ni_3Fe-LDH; in addition, Ni felt peaks for (111) and (200) at 2Θ values of ≈44 and 50 were observed. No other contaminative crystalline phases were detected. Minor contributions of Ni- and Fe- oxides and oxyhydroxides could not be fully excluded due to the overlapping of the possible peaks. After 1000 h of operation, all peaks remained for the NiFe-LDH material. The two peaks at 11° and 23° became more intense, which originated from the overlapping of the NiFe-LDH and NiOOH peaks, as a result of the NiOOH species formed under electrochemical conditions. The flat shoulder-like peak at ≈25°, which is visible starting from 500 h (Figure S12, Supporting Information), also indicates the presence of NiOOH species. The full distinction between individual phases that have formed in between, such as NiOOH, FeOOH, or Fe oxides, is not precisely possible, as the individual peaks overlap and therefore cannot be kept apart, as indicated by the reference pattern (Figure 6A, bottom). The formation of mixed structures is expected as the catalyst layer structure is inhomogeneous and so gradually occurring oxidation steps are presumed. To underline this observation, Raman spectroscopy was further used.

Raman spectra of the pristine aPTEs, after 100, 200, 500, and 1000 h of operation, are presented in Figure 6B. The pristine electrode shows several peaks distributed across the entire measured interval, which claims the presence of mixed oxide and hydroxide structures of Ni with oxidation states from 0 to 3+, contaminating the pure Ni_3Fe-LDH species. Two overlapping bands at 420 and 460 cm^{-1}, a triple peak system at ≈510, 540, and 560 cm^{-1}, and bands ≈600 up to 650 cm^{-1}, are weakly-resolved and most probably highly disturbed by possible anion-conducting binder peaks, as the binder coverage at the catalyst surface is highest for the pristine aPTE. The bands ≈510, 600 cm^{-1} correspond to β-$Ni(OH)_2$, whereas the weak band ≈460 cm^{-1} may come from α-$Ni(OH)_2$, with both hydroxides prepared from an $Ni(NO_3)_2$ reagent.[126] NO_3^- anion residues are reflected in peaks ≈720 and 840 cm^{-1}.[126] Broad hill-like bands ≈460 and 550 cm^{-1} are attributed to the lattice vibrations of the LDH structure.[127] After 100 and 200 h of single-cell operation, the surface undergoes a major change. The NiFe-LDH species become obvious, and representative bands ≈460 and 530 cm^{-1} appear, which are characteristic of the Fe^{3+}/Ni^{2+}—O—Ni^{2+} and Fe^{3+}—O—Fe^{3+}

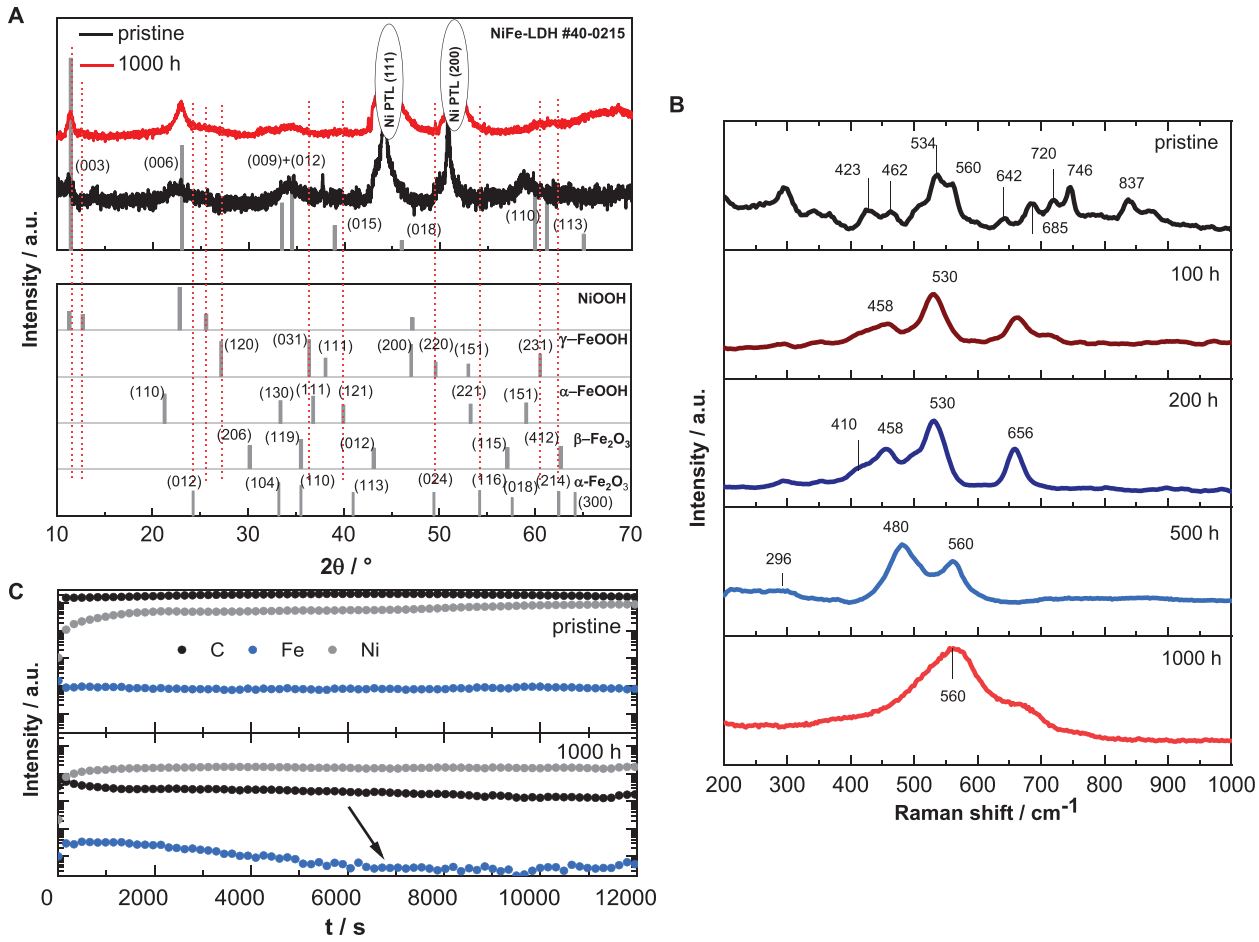

Figure 6. A) XRD pattern, B) Raman spectra, C) ToF-SIMS depth profile of the aPTE samples at different times of the single-cell operation.

bonds.[128,129] Usually, the peak for the intercalating CO_3^{2-} anion is observed at 670–700 cm^{-1}.[31,126,130] Here, we observe a peak at 660 cm^{-1}. The shift to lower wavenumbers is an indication of reduced symmetry from D_{3h} to possibly C_{2V} or C_3, as described elsewhere.[130] Minor bands at 295 and 710 cm^{-1}, which are attributed to the brucite structure, are also visible. After 500 h of single-cell operation, two clear peaks emerged at 480 and 560 cm^{-1}, indicating oxidation of $Ni(OH)_2$ to γ-NiOOH.[127,131] The band at 480 cm^{-1} is attributed to the polarized stretching mode A_{1g} and the 560 cm^{-1} band to the depolarized bending mode E_g of γ-NiOOH.[44] This correlates well with the R_{ct} behavior during the long-term operation time (Figure 3A), which stabilizes after 300 h, also indicating a formation of highly active species like γ-NiOOH. After 1000 h, two broad bands are observed at higher Raman shifts of 560 and 680 cm^{-1}. Here, the bands for γ-FeOOH and γ-NiOOH seem to overlap, containing signals for both species, 526 and 690 cm^{-1}[132-134] for surface γ-FeOOH and the bonds at 480 and 560 cm^{-1}, corresponding to the Ni—O bending and stretching vibrations of NiOOH. The shoulder at 700–900 cm^{-1}, corresponding to $Ni(OH)_2$ disappears. The Raman analysis proves the transition from NiFe-LDH, with some Fe oxide impurities, to full Ni(Fe)OOH. These results, achieved via Raman spectroscopy, correlate well with those obtained by means of XRD.

The X-ray photoelectron spectroscopy (XPS) high-resolution spectra of Ni 2p, Fe 2p and O.1s are shown in Figure S13 (Supporting Information). For Ni 2p pristine, a spectrum of higher loaded aPTE was used, as the binder film on the aPTE surface weakened the XPS signal (Figure S14, Supporting Information). The fitted peak parameters, including the positions (eV) and expected formed species, are summarized in Table S3 (Supporting Information). The single-cell operation time-dependent shifts of the fitted peaks are displayed in Figure S15 (Supporting Information). The overall observation is, that with increasing single-cell operation time, the Ni valence state changed from 2+ to 3+ by forming the Ni oxyhydroxide phase, which is in strong alignment with the Raman spectroscopy data. Additional discussion has been included in the Supporting Information section.

To complement the previous data and further investigate the changes within the catalyst layer, a depth-dependent TOF–SIMS analysis was performed. Figure 6C shows the results for the initial and the 1000 h samples, all intermediate states are presented in Figure S16 (Supporting Information). Thereby, the catalyst layer was continuously sputtered and the released ions were detected. The counts corresponding to Fe- or Ni-containing ions were those of the catalyst (Fe^{x+}, Ni^{x+}), whereas the C-containing ones were assigned to the anion-conducting binder compound. The counts are plotted against the sputtering time, where 1–3 µm

of catalyst layer are removed within 3600 s, and so up to 10 µm of the layer are visible. The TOF–SIMS analysis was supposed to prove the observation of Fe leaching and characterize changes in the anion-conducting binder distribution within the catalyst layer during 1000 h of operation. For all aPTEs, Ni (gray) was observed to be nearly evenly distributed across the depth of the catalyst layer. The overall amount, indicated by the intensity, decreased insignificantly with operation time, which stands in good agreement with the morphological results described previously. Fe (blue) was found to drastically decrease from pristine aPTE to the 1000 h sample, which correlates with the EDX and ICP data presented above and underlines the partial Fe leaching out of the anode catalyst layer. Interestingly, the distribution of Fe decreases from the surface to the bulk of the layer. Fe may be supplied to the outer catalyst layer by redepositing Fe from the electrolyte, whereas only a permanent loss of Fe is possible in the inner layer. The limit of Fe leaching, as well as the recomposing mechanism in relation to catalyst structure and morphology, as well as electrolyte impurities, could be interesting topics of study in the future, but are beyond the scope of this work. As is shown in Figure S16 (Supporting Information), the intensity for the carbon signal (C, black) was notably reduced already after 500 h of steady state operation, indicating a relative reduction in the binder compound content. Either the partial dissolution due to the given electrode structure in terms of inhomogeneous catalyst-binder distribution or the partial delamination of surficial layers upon disassembly of the MEA (Figure S9, Supporting Information) can be considered as possible effects, but need further investigations in the future.

In summary, we were able to prove the stable LDH structure by means of XRD analysis and track the gradual oxidation process from Ni_3Fe-LDH to NiFeOOH via Raman spectroscopy. The altering of the electronic configuration and valence state of Ni during electrolysis could be revealed using XPS. ToF–SIMS analysis emphasized the bulk leaching and possible surface enrichment of Fe, whereas reduction of the anion-conducting binder was recognized. We could therefore present the intersection of surface and bulk composition (as morphological changes) of the Ni_3Fe-LDH anode and their chemical changes in terms of the electrochemical behavior of the single-cell. The analysis of the morphological changes and oxidation states of present species at each point of operation time could explain the change in the internal resistances of the cell, as Ohmic (R_{Ohm}) and charge-transfer resistance (R_{ct}), which is explained in the first part of the Discussion.

The potential influences of the cathode side, as well as changes in the PTL supports and AEM, could ideally be considered, but this would be beyond this work's scope. The leaching of Fe, reduction of the anion-conducting binder compound, and the morphological reconstruction of the catalyst layer were observed to occur during the 1000 h operation under industrial conditions.[66,94] Taking all of these factors into account, the Ni_3Fe-LDH-based aPTE exhibits highly promising results.

3. Conclusion

In this study, the performance and stability of an MEA based on the Ni_3Fe-LDH OER catalyst and the AEM DURAION by Evonik, along with its corresponding preliminary anion-conducting binder, were investigated. The single-cell achieved excellent performance of 2 A cm^{-2} at 2 V, exhibiting a stable and low-cost MEA for future applications in AEMWEs. The stationary long-term durability of 1000 h, with a minor degradation rate of 84 µV h^{-1} after a break-in (conditioning) time, could, moreover, be reproducibly proven. Additionally, the importance of a sufficient operation time was validated, when reporting long-term tests, as the catalyst conditioning time may take hundreds of hours.

Furthermore, the degradation mechanism of the Ni_3Fe-LDH aPTE was systematically tracked by a variety of characterization methods. By in situ impedance spectroscopy, correlated with the single-cell voltage trend, the electrocatalytic activity of the MEA was found to increase for the first 200 h and slightly decrease afterward. The changes were attributed to the formation of different conductive phases, as proven by Raman spectroscopy. Starting with mixed oxides and hydroxides, after 100 h of operation, NiFe-LDH is found, further oxidized into γ-NiOOH, and finally into Ni(Fe)OOH, which is probably a mixture of γ-NiOOH and amorphous FeOOH. Being operated in a real electrolyzer environment, the catalyst within the aPTE experiences deficiencies comparable to those of non-bounded catalyst powder. Monitoring of the aPTE state during the operation lifetime revealed a continuous anion-conducting binder release and Fe dissolution, reaching up to 43% after 1000 h. Regardless of the leaching phenomenon, no significant increase in cell potential was observed during the tested period. The post-mortem HR–TEM analysis revealed that the catalyst was not fully amorphous, but the LDH nano-sheets were still recognizable, while a mixed structure of crystallite and amorphous regions could be observed. A deep reconstruction of the catalyst layer was revealed by SEM analysis, which was conducted between 500 and 1000 h of operation. The reorganization occurred due to the formation of oxyhydroxides and crystalline mixed regions. The aPTE showed a partial crack formation after the long-term test; nevertheless, bigger catalyst layer detachments were not observed.

The presented aPTE preparation method is simple and scalable, allowing for the development of large-scale non-PGM electrodes with a stable structure, which is important for the AEMWE technology in order to scale up and progress. This study helps fill the gap between academic and industrial mindsets, presenting a stable, inexpensive Ni_3Fe-LDH-based electrolyzer cell.

4. Experimental Section

Chemicals and Materials: The Ni_3Fe-LDH catalyst was synthesized by means of the co-precipitation method based on the low solubility product of metal ions (Ni^{2+} and Fe^{3+}) in alkaline solution, as described elsewhere.[54] The multilayer structure of the Ni_3Fe-LDH consists of several stacked hydroxide single layers and intercalated NO_3^- and CO_3^{2-} anions (Figure S17, Supporting Information). The layered structure morphology was examined using transmission electron microscopy (TEM), as depicted in Figure S18 (Supporting Information). On the cathode side, commercial Pt/C (60% high surface area carbon, Alfa Aesar) was used, whereas for PGM-based anodes, commercial Ir black powder (99.8% metals basis, Alfa Aesar) was used. All aqueous solutions were prepared using Milli-Q water (18.2 MΩ, EMD Millipore). The anion exchange membrane DURAION and its corresponding preliminary anion-conducting binder were supplied by Evonik (AEM with ≈70 µm wet thickness). Nickel fiber substrate with a porosity of 66% and a highly conductive connected network of Ni fibers with a diameter of 22 µm, with an overall porous transport layer (PTL) thickness of 500 µm (Ni 2GDL30-0.50, Bekaert), was used as the PTL on the anode side, whereas carbon fiber composite paper (TGP–H–120,

370 µm-thick, Toray) was used as the cathode PTL. For 1 M KOH electrolyte preparation, solid pellets were used (EMSURE, 85% purity KOH, VWR).

Electrode and MEA Fabrication: For Ni_3Fe-LDH ink formulation, 500 mg of catalyst was mixed with 15.5 mg of DI water and dispersed for 5 min at 4000 rpm with a rotating disperser tool (IKA Ultra-Turrax). Furthermore, 2500 mg of 5 wt% binder solution and 15.5 mg of EtOH were added, followed by an additional 5 min of Ultra-Turrax dispersing. Final homogenization was achieved with 30 min of ultrasonic horn treatment (SONOPULS ultrasonic homogenizer by BANDELIN electronic GmbH & Co. KG), while cooling of the dispersion took place inside an ice bath. For Ir anodes, 500 mg of catalyst, 2600 mg of 5 wt% binder solution, and 40.4 mg of both DI water and EtOH, were mixed and dispersed in the same way. The cathode Pt/C formulations were prepared in the same way, by mixing 500 mg of catalyst and 3333.4 mg of 5 wt% binder solution, DI water and EtOH, each 40.4 mg. The total solid content of the catalyst and anion-conducting binder in the catalyst inks was 2 wt%, the binder comprised 20 and 25 wt% of total solid content for the Ni_3Fe-LDH and Pt/C inks, respectively.

The catalyst-coated substrate (CCS) configuration was chosen for MEA fabrication; the catalyst was then directly applied on the PTL forming porous-transport electrodes (PTEs). The AEM was sandwiched between two PTEs without additional hot pressing. The CCS arrangement was selected, as it has several advantages for the system: i) replacement of difficult configurations containing gas diffusion layers and microporous transport layers on self-supported electrodes; ii) the catalyst was distributed not only on one plain surface but coats several fibers, distributing the PTL bulk and forming a larger electrochemical surface, increasing the catalyst utilization; and iii) direct contact between the highly conductive Ni PTL and catalyst layer formed a stable structure that reduces mass transport losses while promoting electrical conductivity.[24,135,136]

The electrodes were prepared with the ultrasonic spray deposition method using an automatic spray coater (Exactacoat by SONO–TEK) (Figure S19, Supporting Information). Prior to spray coating, the precut PTLs were fixed on an 80 °C heated vacuum plate. A stainless steel frame prevented the PTLs from occasional movements. The catalyst ink was deposited layer by layer onto the PTLs by a meander-shaped path. To ensure a high level of homogeneity, the layers were sprayed in both the x- and y-directions with positive and negative offsets of one-third of the sprayed line width (Figure S20, Supporting Information). On the anode side, a Ni_3Fe-LDH loading of 2 mg cm^{-2} was reached (or 1 mg cm^{-2} for the comparative tests with the Ir-based singe cell); on the cathode side, 0.6 mg_{Pt} cm^{-2} of catalyst was deposited. For the Ir anodes, a loading of 1 mg cm^{-2} was chosen. The exact catalyst loading was gravimetrically monitored via weight increases of a reference sample that was coated in parallel with the PTE. Prior to single-cell assembly, the membrane and both the anode and cathode PTEs were soaked in 1 M of KOH electrolyte for pre-conditioning. The MEA components were then assembled in a wet state at room temperature.

Single-cell Assembly and Electrochemical Measurements: All electrochemical measurements were operated in an in-house cell hardware with an active area of 5 cm^2 and nickel meander flow-fields on both sides. The single-cell set-up, including the MEA design, used in this work is presented in Figure 1A. MEA compression was ensured by PTFE foils used as sealing, which were 250 µm-thick on the cathode side and 500 µm-thick on the anode one. To prevent any electrical contact between the conductive components, reinforced PTFE foils were positioned between the stainless steel end plates and flow-fields. For system heating, including the single-cell and electrolyte, heating rods were connected to both flow-fields. The cell temperature was set to 60 °C and controlled by a thermocouple that was connected to the cell and thermostat. The anode and cathode sides were fed separately with a 1 M KOH electrolyte and water at a flow rate of 10 mL min^{-1} cm^{-2}, while membrane pumps were used for electrolyte circulation during the measurement. A water supply with a level sensor (TURCK GmbH & Co. KG) ensured a constant electrolyte concentration in the system. Before connecting the single-cells, nitrogen gas was percolated through the test station, including the electrolyte tanks with electrolytes inside, for degassing for at least 2 h. For all electrochemical tests, the battery cycler potentiostat workstation (BioLogic Science Instruments, BT-815, 15 A max., 10 kHz max.) was employed. The parameters for all single-cell tests and conditions are summarized in Table S4 (Supporting Information).

The measurement protocol was chosen according to the EU harmonized measurement protocol for low-temperature water electrolysis.[137] Starting with a 3 h open circuit voltage step for electrolyte heating and electrolyte equilibration between the cells and test station, a break-in step was performed as a linear voltammetry sweep with a scan rate of 5 mV s^{-1} at 1.4–2.1 V and a conditioning step at a constant current of 1 A cm^{-2} for 4 h. The fast linear current sweep verified the functionality of the cell and acted as a short-circuit check, whereas the controlled constant current step activated the catalysts. Holding constant current values from 0.016 up to 2 A cm^{-2} for 1 min (with a step of 0.016 A cm^{-2} from 0.016 to 0.12 A cm^{-2}, a step of 0.02 A cm^{-2} from 0.12 to 0.2 A cm^{-2}, 0.05 A cm^{-2} between 0.2 and 1.4 A cm^{-2} and 0.1 up to 3 A cm^{-2}), a polarization curve was recorded. The voltage limit was set to 2.1 V, and two consecutive polarization curves were recorded. The second current–voltage curve was chosen as the one for evaluation, validating that the cell was fully conditioned. This was proved by the comparison of first and second polarization curves, which should be equal. Afterward, galvanostatic impedance spectroscopy (GEIS) measurements were performed at 20 points at current densities of between 40 mA cm^{-2} and 2 A cm^{-2} with an amplitude of 10% DC and a frequency range of 0.1 Hz–10 kHz. The corresponding current densities were held for 5 min each before the GEIS analysis. The high-frequency resistances (HFRs, R_{ct}) were used for further iR correction of the polarization curve, whereas the Nyquist plots at 500 mA cm^{-2} are presented and discussed in this work. This measurement protocol resulted in a short-term single-cell performance test (15 h) containing a break-in procedure. By including loops in the measurement protocol with a holding of 1 A cm^{-2} for 100 h in between the polarization curves and GEIS measurements, a 1000 h long-term operation test was performed.

For evaluating the results of the impedance spectroscopy, the program BT-lab V 1.75 (BioLogic BT-Lab Software) was employed. The equivalent circuit for data fitting consisted of two parallel circuits in series, each comprising a resistor and constant phase element (CPE), in series with a resistor as used elsewhere (Figure S21, Supporting Information).[68,138–140] The obtained Nyquist plots were fitted three times, simulating the Ohmic resistances (R_{Ohm}) and so-called charge transfer resistances (R_{ct}) three times; the average values were discussed.

To calculate the voltage efficiency η_{HVV}, Equations S1.1–S1.3 (Supporting Information)[30] were used with E° of 1.199 V being the theoretical thermodynamic potential of water electrolysis at 60 °C.

Physical and Chemical Characterization: The structural characterization of the anode PTEs was confirmed by X-ray diffraction (XRD) using a D8 Discovery X-ray Diffractometer with Cu-Kα radiation (0.154 nm) in Bragg–Brentano geometry. The diffractograms were recorded in the 2θ range from 5° to 70°. Scanning electron microscopy (SEM) (a Zeiss Gemini Ultra Plus device) was used for catalyst morphology examination of the PTEs using AsB, SE2, Inlens signal detection, and a 2–20 kV operational voltage.

Energy dispersive X-ray analysis (EDX) was performed using the Zeiss Gemini Ultra Plus device at a 20 kV operational voltage for an elemental composition study.

X-ray photoemission spectroscopy (XPS) was used as a tool to explore catalyst surface composition on the PTEs using a Kratos Axis Ultra DLD device with monochromatic Al X-ray source (1.486 keV). The survey spectra were obtained at 187.5 eV pass energy, 0.8 eV per step, and 100 ms per step. The detailed core-level spectra were recorded with a pass energy of 23.5 and 0.1 eV per step. Charge-correction was conducted by setting the C—C 1s bond peak to 285 eV.

Ex situ Raman spectroscopy was carried out using the WITec alpha300 R confocal Raman device, equipped with a 532 nm laser. The aperture was fixed at 50 × 1000 µm, the spectral resolution was ≈1 cm^{-1}, the single spectrum was accumulated at an integration time of 3 s, and the obtained signals were averaged over a few single scans.

A Focused Ion Beam (FIB) with FEI Helios NanoLab 460F1 device was used to cut one catalyst-coated fiber of the PTL and image high-resolution cross-sectional SEM images. The FIB was used, moreover, for

transmission electron microscopy (TEM) lamellar sample preparation. The samples were treated in a 10^{-7} bar vacuum environment.

To confirm the stable LDH structure, TEM and high resolution TEM (HR–TEM) images were obtained using an FEI Titan, 80–300 TEM, with a Cs corrector for the objective lens (CEOS GmbH).[141] The microscope was operated at 300 kV.

Inductively-coupled plasma coupled with mass spectrometry (ICP–MS) on an Agilent 7900 device was used for electrolyte element analysis. Each electrolyte sample was 100-fold diluted, three replicates of one sample were tested, and the analyzed data was averaged, resulting in a μg L^{-1} quantity of element.

Scanning transmission electron microscopy (STEM) imaging and energy-dispersive spectrometry (EDS) mapping were conducted with a Thermo Scientific Titan 80–200 electron microscope equipped with a probe corrector (CEOS) and a high angle annular dark field (HAADF) detector. "Z-contrast" conditions were achieved by implementing a probe semi-angle of 30 mrad and an inner collection angle of the detector of 75 mrad.[142]

For the lattice fraction calculations, the DigitalMicrograph 3.7.4. program from Gatan Inc. was used. The obviously visible patterns were analyzed by the contrast extraction tool and confirmed with the Reduced *FFT* tool.

A time-of-flight secondary ion mass spectrometry (TOF–SIMS) in depth-profile analysis was used to analyze the elemental amounts inside the catalyst layer, such as Ni, Fe, and C. For analysis, the instruments IONTOF TOF–SIMS 5.ncs, including the microscope Camera LEAP 4000 3D-Atomprobe, were used. An average sputtering time of 12 000 s was measured, which corresponds to a depth of ≈10 μm. Cs ions were also used for sputtering.

Statistical Analysis: For values presented with an associated error or when error bars were described, the data was represented as the mean value ± standard deviation (SD). These values were derived from a minimum of three experimental data sets to ensure accuracy. Microsoft Office Excel was employed for the calculation of both the mean and the SD.

Supporting Information

Supporting Information is available from the Wiley Online Library or from the author.

Acknowledgements

This project received funding from the Fuel Cells and Hydrogen 2 Joint Undertaking under grant agreement No 875088. This Joint undertaking received support from the European Union's Horizon 2020 research innovation program, as well as Hydrogen Europe and Hydrogen Europe Research. The authors thank Dr. Heinrich Hartmann for conducting the XPS analysis and to Dr. Felix Lohmann-Richters for his contributions to result-related discussions. Thanks to the Ernst Ruska-Centre for Microscopy and Spectroscopy with Electrons (ER-C) for conducting the fib-SEM analysis.

Open access funding enabled and organized by Projekt DEAL.

Conflict of Interest

The authors declare no conflict of interest.

Data Availability Statement

The data that support the findings of this study are available from the corresponding author upon reasonable request.

Keywords

anion exchange membrane water electrolysis, catalyst layers, electrode degradation studies, electrolyzer durability, NiFe LDH catalysts, post-mortem analysis, water electrolysis

Received: December 1, 2023
Revised: December 14, 2023
Published online: January 25, 2024

[1] D. Apostolou, P. Enevoldsen, G. Xydis, *Int. J. Hydrogen Energy* **2019**, *44*, 9675.
[2] Hydrogen Applications. Hydrogen Europe, https://hydrogeneurope.eu/hydrogen-applications.(accessed: November 2020).
[3] S. van Renssen, *Nat Clim Chang* **2020**, *10*, 799.
[4] IPCC, 2018: Summary for Policymakers. In: Global Warming of 1.5°C. An IPCC Special Report on the impacts of global warming of 1.5°C above pre-industrial levels and related global greenhouse gas emission pathways, in the context of strengthening the global response to the threat of climate change, sustainable development, and efforts to eradicate poverty, (Eds.: V. Masson-Delmotte, P. Zhai, H.-O. Pörtner, D. Roberts, J. Skea, P. R. Shukla, A. Pirani, W. Moufouma-Okia, C. Pe9˜an, R. Pidcock, S. Connors, J. B. R. Matthews, Y. Chen, X. Zhou, M. I. Gomis, E. Lonnoy, T. Maycock, M. Tignor, T. Waterfield), World Meteorological Organization, Geneva, Switzerland, p. 32.
[5] S. Shiva Kumar, V. Himabindu, *Mater Sci Energy Technol* **2019**, *2*, 442.
[6] J. Brauns, T. Turek, *Processes* **2020**, *8*, 248.
[7] Critical raw materials, https://ec.europa.eu/growth/sectors/raw-materials/areas-specific-interest/critical-raw-materials_en (accessed: March 2023).
[8] G. Schiller, R. Henne, P. Mohr, V. Peinecke, *Int. J. Hydrogen Energy* **1998**, *23*, 761.
[9] M. Schalenbach, G. Tjarks, M. Carmo, W. Lueke, M. Mueller, D. Stolten, *J. Electrochem. Soc.* **2016**, *163*, F3197.
[10] M. Carmo, D. L. Fritz, J. Mergel, D. Stolten, *Int. J. Hydrogen Energy* **2013**, *38*, 4901.
[11] M. F. Lagadec, A. Grimaud, *Nat. Mater.* **2020**, *19*, 1140.
[12] C. Tang, N. Cheng, Z. Pu, W. Xing, X. Sun, *Angew. Chem.* **2015**, *127*, 9483.
[13] G. Wang, J. Li, M. Liu, L. Du, S. Liao, *ACS Appl. Mater. Interfaces* **2018**, *10*, 32133.
[14] I. H. Kwak, H. S. Im, D. M. Jang, Y. W. Kim, K. Park, Y. R. Lim, E. H. Cha, J. Park, *ACS Appl. Mater. Interfaces* **2016**, *8*, 5327.
[15] B. M. Hunter, H. B. Gray, A. M. Muller, *Chem. Rev.* **2016**, *116*, 14120.
[16] D. Xu, M. B. Stevens, M. R. Cosby, S. Z. Oener, A. M. Smith, L. J. Enman, K. E. Ayers, C. B. Capuano, J. N. Renner, N. Danilovic, Y. Li, H. Wang, Q. Zhang, S. W. Boettcher, *ACS Catal.* **2019**, *9*, 7.
[17] A. Y. Faid, A. O. Barnett, F. Seland, S. Sunde, *Catalysts* **2018**, *8*, 614.
[18] T. Hosaka, K. Kubota, A. S. Hameed, S. Komaba, *Chem. Rev.* **2020**, *120*, 6358.
[19] M. Gong, H. Dai, *Nano Res.* **2014**, *8*, 23.
[20] A. Y. Faid, A. O. Barnett, F. Seland, S. Sunde, *J. Electrochem. Soc.* **2019**, *166*, F519.
[21] X. Yu, M. Zhang, W. Yuan, G. Shi, *J. Mater. Chem. A* **2015**, *3*, 6921.
[22] P. Thangavel, M. Ha, S. Kumaraguru, A. Meena, A. N. Singh, A. M. Harzandi, K. S. Kim, *Energy Environ. Sci.* **2020**, *13*, 3447.
[23] J. Lee, H. Jung, Y. S. Park, S. Woo, J. Yang, M. J. Jang, J. Jeong, N. Kwon, B. Lim, J. W. Han, S. M. Choi, *Small* **2021**, *17*, 2100639.
[24] J. Xiao, A. M. Oliveira, L. Wang, Y. Zhao, T. Wang, J. Wang, B. P. Setzler, Y. Yan, *ACS Catal.* **2021**, *11*, 264.
[25] S. S. Jeon, J. Lim, P. W. Kang, J. W. Lee, G. Kang, H. Lee, *ACS Appl. Mater. Interfaces* **2021**, *13*, 37179.
[26] S. Yin, W. Tu, Y. Sheng, Y. Du, M. Kraft, A. Borgna, R. Xu, *Adv. Mater.* **2018**, *30*, 1705106.

[27] Q. Wang, L. Shang, R. Shi, X. Zhang, Y. Zhao, G. I. N. Waterhouse, L. Z. Wu, C. H. Tung, T. Zhang, *Adv. Energy Mater.* **2017**, *7*, 1700467.
[28] Z. Lu, W. Xu, W. Zhu, Q. Yang, X. Lei, J. Liu, Y. Li, X. Sun, X. Duan, *Chem. Commun.* **2014**, *50*, 6479.
[29] S. C. Zignani, M. Lo Faro, S. Trocino, A. S. Aricò, *Energies* **2020**, *13*, 1720.
[30] H. Koshikawa, H. Murase, T. Hayashi, K. Nakajima, H. Mashiko, S. Shiraishi, Y. Tsuji, *ACS Catal.* **2020**, *10*, 1886.
[31] Z. W. Gao, J. Y. Liu, X. M. Chen, X. L. Zheng, J. Mao, H. Liu, T. Ma, L. Li, W. C. Wang, X. W. Du, *Adv. Mater.* **2019**, *31*, 1804769.
[32] D. Zhou, S. Wang, Y. Jia, X. Xiong, H. Yang, S. Liu, J. Tang, J. Zhang, D. Liu, L. Zheng, Y. Kuang, X. Sun, B. Liu, *Angew. Chem., Int. Ed.* **2019**, *58*, 736.
[33] R. Chen, S. F. Hung, D. Zhou, J. Gao, C. Yang, H. Tao, H. B. Yang, L. Zhang, L. Zhang, Q. Xiong, H. M. Chen, B. Liu, *Adv. Mater.* **2019**, *31*, 1903909.
[34] Q. Xiang, F. Li, W. Chen, Y. Ma, Y. Wu, X. Gu, Y. Qin, P. Tao, C. Song, W. Shang, H. Zhu, T. Deng, J. Wu, *ACS Energy Lett.* **2018**, *3*, 2357.
[35] J. Mohammed-Ibrahim, *J. Power Sources* **2020**, *448*, 227375.
[36] F. Dionigi, P. Strasser, *Adv. Energy Mater.* **2016**, *6*, 1600621.
[37] J. Luo, J. H. Im, M. T. Mayer, M. Schreier, M. K. Nazeeruddin, N. G. Park, S. D. Tilley, H. J. Fan, M. Grätzel, *Science* **2014**, *345*, 1593.
[38] L. Trotochaud, S. L. Young, J. K. Ranney, S. W. Boettcher, *J. Am. Chem. Soc.* **2014**, *136*, 6744.
[39] Z. Li, M. Shao, H. An, Z. Wang, S. Xu, M. Wei, D. G. Evans, X. Duan, *Chem. Sci.* **2015**, *6*, 6624.
[40] M. Görlin, P. Chernev, J. F. De Araújo, T. Reier, S. Dresp, B. Paul, R. Krähnert, H. Dau, P. Strasser, *J. Am. Chem. Soc.* **2016**, *138*, 5603.
[41] M. W. Louie, A. T. Bell, *J. Am. Chem. Soc.* **2013**, *135*, 12329.
[42] D. Friebel, M. W. Louie, M. Bajdich, K. E. Sanwald, Y. Cai, A. M. Wise, M. J. Cheng, D. Sokaras, T. C. Weng, R. Alonso-Mori, R. C. Davis, J. R. Bargar, J. K. Nørskov, A. Nilsson, A. T. Bell, *J. Am. Chem. Soc.* **2015**, *137*, 1305.
[43] X. Zhang, Y. Zhao, Y. Zhao, R. Shi, G. I. N. Waterhouse, T. Zhang, *Adv. Energy Mater.* **2019**, *9*, 1802832.
[44] S. Lee, L. Bai, X. Hu, *Angew. Chem., Int. Ed.* **2020**, *59*, 8072.
[45] F. Dionigi, J. Zhu, Z. Zeng, T. Merzdorf, H. Sarodnik, M. Gliech, L. Pan, W. X. Li, J. Greeley, P. Strasser, *Angew. Chem., Int. Ed.* **2021**, *60*, 14446.
[46] Q. Wang, D. Ohare, *Chem. Rev.* **2012**, *112*, 4124.
[47] J. Lee, H. Jung, Y. S. Park, S. Woo, N. Kwon, Y. Xing, S. H. Oh, S. M. Choi, J. W. Han, B. Lim, *Chem. Eng. J.* **2021**, *420*, 127670.
[48] I. Vincent, E. C. Lee, H. M. Kim, *RSC Adv.* **2020**, *10*, 37429.
[49] R. R. Raja Sulaiman, W. Y. Wong, K. S. Loh, *Int. J. Energy Res.* **2022**, *46*, 2241.
[50] H. Jin, B. Ruqia, Y. Park, H. J. Kim, H. S. Oh, S. Il Choi, K. Lee, *Adv. Energy Mater.* **2021**, *11*, 2003188.
[51] M. J. Jang, J. Yang, J. Lee, Y. S. Park, J. Jeong, S. M. Park, J. Y. Jeong, Y. Yin, M. H. Seo, S. M. Choi, K. H. Lee, *J. Mater. Chem. A* **2020**, *8*, 4290.
[52] Y. S. Park, M. J. Jang, J. Jeong, S. M. Park, X. Wang, M. H. Seo, S. M. Choi, J. Yang, *ACS Sustainable Chem. Eng.* **2020**, *8*, 2344.
[53] A. Y. Faid, H. Ismail, *Mater. Today Energy* **2019**, *13*, 285.
[54] W. Jiang, A. Y. Faid, B. F. Gomes, I. Galkina, L. Xia, C. M. S. Lobo, M. Desmau, P. Borowski, H. Hartmann, A. Maljusch, A. Besmehn, C. Roth, S. Sunde, W. Lehnert, M. Shviro, *Adv. Funct. Mater.* **2022**, *32*, 2203520.
[55] T. Zhan, X. Liu, S. S. Lu, W. Hou, *Appl Catal B* **2017**, *205*, 551.
[56] M. K. Bates, Q. Jia, N. Ramaswamy, R. J. Allen, S. Mukerjee, *J. Phys. Chem. C* **2015**, *119*, 5467.
[57] T. H. Pham, J. S. Olsson, P. Jannasch, *J. Am. Chem. Soc.* **2017**, *139*, 2888.
[58] T. Y. Son, T. H. Kim, S. Y. Nam, *Polymers* **2020**, *12*, 2758.
[59] P. Fortin, T. Khoza, X. Cao, S. Y. Martinsen, A. Oyarce Barnett, S. Holdcroft, *J. Power Sources* **2020**, *451*, 227814.
[60] Z. Zhang, K. Shen, L. Lin, J. Pang, *J. Membr. Sci.* **2016**, *497*, 318.
[61] X. Chu, Y. Shi, L. Liu, Y. Huang, N. Li, *J. Mater. Chem. A* **2019**, *7*, 7717.
[62] D. Henkensmeier, M. Najibah, C. Harms, J. Žitka, J. Hnát, K. Bouzek, *J. Electrochem. Energy Convers. Storage* **2021**, *18*, 024001.
[63] T. Huang, G. He, J. Xue, O. Otoo, X. He, H. Jiang, J. Zhang, Y. Yin, Z. Jiang, J. C. Douglin, D. R. Dekel, M. D. Guiver, *J. Membr. Sci.* **2020**, *597*, 117769.
[64] L. Wang, M. Bellini, H. A. Miller, J. R. Varcoe, *J. Mater. Chem. A* **2018**, *6*, 15404.
[65] E. Cossar, F. Murphy, E. A. Baranova, *J. Chem. Technol. Biotechnol.* **2022**, *97*, 1611.
[66] N. Du, C. Roy, R. Peach, M. Turnbull, S. Thiele, C. Bock, *Chem. Rev.* **2022**, *122*, 11830.
[67] H. Qi, P. Zhang, H. Wang, Y. Cui, X. Liu, X. She, Y. Wen, T. Zhan, *J. Colloid Interface Sci.* **2021**, *599*, 370.
[68] A. Y. Faid, A. O. Barnett, F. Seland, S. Sunde, *ACS Appl. Energy Mater.* **2021**, *4*, 3327.
[69] I. Vincent, A. Kruger, D. Bessarabov, *Int. J. Electrochem. Sci.* **2018**, *13*, 11347.
[70] A. Mavrič, C. Cui, *ACS Appl. Energy Mater.* **2021**, *4*, 12032.
[71] L. Wang, V. A. Saveleva, M. J. Eslamibidgoli, D. Antipin, C. Bouillet, I. Biswas, A. S. Gago, S. S. Hosseiny, P. Gazdzicki, M. H. Eikerling, E. R. Savinova, K. A. Friedrich, *ACS Appl. Energy Mater.* **2022**, *5*, 2221.
[72] A. K. Niaz, A. Akhtar, J. Y. Park, H. T. Lim, *J. Power Sources* **2021**, *481*, 229093.
[73] L. A. King, M. K. A. Hubert, C. Capuano, J. Manco, N. Danilovic, E. Valle, T. R. Hellstern, K. Ayers, T. F. Jaramillo, *Nat. Nanotechnol.* **2019**, *14*, 1071.
[74] M. J. Jang, S. H. Yang, M. G. Park, J. Jeong, M. S. Cha, S. Shin, K. H. Lee, Z. Bai, Z. Chen, J. Y. Lee, S. M. Choi, *ACS Energy Lett.* **2022**, *7*, 2576.
[75] I. Vincent, D. Bessarabov, *Renew Sustain Energy Rev* **2018**, *81*, 1690.
[76] P. M. Bodhankar, P. B. Sarawade, G. Singh, A. Vinu, D. S. Dhawale, *J. Mater. Chem. A* **2021**, *9*, 3180.
[77] M. Bernt, H. A. Gasteiger, *J. Electrochem. Soc.* **2016**, *163*, F3179.
[78] A. Lim, H. juhn Kim, D. Henkensmeier, S. Jong Yoo, J. Young Kim, S. Young Lee, Y. E. Sung, J. H. Jang, H. S. Park, *J Ind Eng Chem* **2019**, *76*, 410.
[79] M. K. Cho, H. S. H. Y. Park, H. J. Lee, H. J. Kim, A. Lim, D. Henkensmeier, S. J. Yoo, J. Y. Kim, S. Y. Lee, H. S. H. Y. Park, J. H. Jang, *J. Power Sources* **2018**, *382*, 22.
[80] M. K. Cho, H. Y. Park, S. Choe, S. J. Yoo, J. Y. Kim, H. J. Kim, D. Henkensmeier, S. Y. Lee, Y. E. Sung, H. S. Park, J. H. Jang, *J. Power Sources* **2017**, *347*, 283.
[81] B. Mayerhöfer, D. McLaughlin, T. Böhm, M. Hegelheimer, D. Seeberger, S. Thiele, *ACS Appl. Energy Mater.* **2020**, *3*, 9635.
[82] G. Huang, M. Mandal, N. U. Hassan, K. Groenhout, A. Dobbs, W. E. Mustain, P. A. Kohl, *J. Electrochem. Soc.* **2020**, *167*, 164514.
[83] C. C. Pavel, F. Cecconi, C. Emiliani, S. Santiccioli, A. Scaffidi, S. CataPavenorchi, M. Comotti, *Angew. Chem., Int. Ed.* **2014**, *53*, 1378.
[84] L. Xiao, S. Zhang, J. Pan, C. Yang, M. He, L. Zhuang, J. Lu, *Energy Environ. Sci.* **2012**, *5*, 7869.
[85] I. Vincent, A. Kruger, D. Bessarabov, *Int. J. Hydrogen Energy* **2017**, *42*, 10752.
[86] Q. Wen, K. Yang, D. Huang, G. Cheng, X. Ai, Y. Liu, J. Fang, H. Li, L. Yu, T. Zhai, *Adv. Energy Mater.* **2021**, *11*, 2102353.
[87] K. Yue, J. Liu, Y. Zhu, C. Xia, P. Wang, J. Zhang, Y. Kong, X. Wang, Y. Yan, B. Y. Xia, *Energy Environ. Sci.* **2021**, *14*, 6546.
[88] D. Li, A. R. Motz, C. Bae, C. Fujimoto, G. Yang, F. Y. Zhang, K. E. Ayers, Y. S. Kim, *Energy Environ. Sci.* **2021**, *14*, 3393.

[89] F. Razmjooei, T. Morawietz, E. Taghizadeh, E. Hadjixenophontos, L. Mues, M. Gerle, B. D. Wood, C. Harms, A. S. Gago, S. A. Ansar, K. A. Friedrich, *Joule* **2021**, *5*, 1776.
[90] A. Khataee, A. Shirole, P. Jannasch, A. Krüger, A. Cornell, *J. Mater. Chem. A* **2022**, *10*, 16061.
[91] J. Xing, Z. Zeng, W. Best, Z. Liu, L. Bonville, R. Maric, S. Bliznakov, *J. Power Sources* **2023**, *558*, 232564.
[92] J. Larminie, A. Dicks, *Fuel Cell Systems Explained*, John Wiley & Sons. Ltd, Hoboken, New Jersey **2003**.
[93] H. A. Miller, K. Bouzek, J. Hnat, S. Loos, C. I. Bernäcker, T. Weißgärber, L. Röntzsch, J. Meier-Haack, *Sustainable Energy Fuels* **2020**, *4*, 2114.
[94] K. Zeng, D. Zhang, *Prog. Energy Combust. Sci.* **2010**, *36*, 307.
[95] C. Zhang, M. Shao, L. Zhou, Z. Li, K. Xiao, M. Wei, *ACS Appl. Mater. Interfaces* **2016**, *8*, 33697.
[96] C. Andronescu, S. Barwe, E. Ventosa, J. Masa, E. Vasile, B. Konkena, S. Möller, W. Schuhmann, *Angew. Chem., Int. Ed.* **2017**, *56*, 11258.
[97] R. Li, J. Xu, Q. Pan, J. Ba, T. Tang, W. Luo, *ChemistryOpen* **2019**, *8*, 1027.
[98] Z. Zhang, D. Zhou, J. Liao, X. Bao, H. Yu, *Int. J. Energy Res.* **2019**, *43*, 1460.
[99] X. Li, F. C. Walsh, D. Pletcher, *Phys. Chem. Chem. Phys.* **2011**, *13*, 1162.
[100] Z. Liu, S. D. Sajjad, Y. Gao, H. Yang, J. J. Kaczur, R. I. Masel, *Int. J. Hydrogen Energy* **2017**, *42*, 29661.
[101] B. Motealleh, Z. Liu, R. I. Masel, J. P. Sculley, Z. R. Ni, L. Meroueh, *Int. J. Hydrogen Energy* **2021**, *46*, 3379.
[102] N. Ul Hassan, M. Mandal, G. Huang, H. A. Firouzjaie, P. A. Kohl, W. E. Mustain, *Adv. Energy Mater.* **2020**, *10*, 1.
[103] S. Siracusano, V. Baglio, S. A. Grigoriev, L. Merlo, V. N. Fateev, A. S. Aricò, *J. Power Sources* **2017**, *366*, 105.
[104] V. Gatard, I. M. Marin, D. De Masi, T. Encinas, F. Charlot, V. Martin, M. Aouine, C. Geantet, S. Faure, J. Deseure, J. Carrey, B. Chaudret, M. Chatenet, *ACS Appl. Energy Mater.* **2022**, *5*, 7034.
[105] A. R. Zeradjanin, A. A. Topalov, Q. Van Overmeere, S. Cherevko, X. Chen, E. Ventosa, W. Schuhmann, K. J. J. Mayrhofer, *RSC Adv.* **2014**, *4*, 9579.
[106] R. A. Krivina, G. A. Lindquist, M. C. Yang, A. K. Cook, C. H. Hendon, A. R. Motz, C. Capuano, K. E. Ayers, J. E. Hutchison, S. W. Boettcher, *ACS Appl. Mater. Interfaces* **2022**, *14*, 18261.
[107] R. A. Krivina, G. A. Lindquist, S. R. Beaudoin, T. N. Stovall, W. L. Thompson, L. P. Twight, D. Marsh, J. Grzyb, K. Fabrizio, J. E. Hutchison, S. W. Boettcher, *Adv. Mater.* **2022**, *33*, 2203033.
[108] S. Koch, P. A. Heizmann, S. K. Kilian, B. Britton, S. Holdcroft, S. Vierrath, M. Breitwieser, S. Vierrath, *J. Mater. Chem. A* **2021**, *9*, 15744.
[109] B. Mayerhöfer, K. Ehelebe, F. D. Speck, M. Bierling, J. Bender, J. A. Kerres, K. J. J. Mayrhofer, S. Cherevko, R. Peach, S. Thiele, *J. Mater. Chem. A* **2021**, *9*, 14285.
[110] P. Oliva, J. Leonardi, J. F. Laurent, C. Delmas, J. J. Braconnier, M. Figlarz, F. Fievet, A. de Guibert, *J. Power Sources* **1982**, *8*, 229.
[111] S. Lee, K. Banjac, M. Lingenfelder, X. Hu, *Angew. Chem., Int. Ed.* **2019**, *58*, 10295.
[112] M. B. Stevens, C. D. M. Trang, L. J. Enman, J. Deng, S. W. Boettcher, *J. Am. Chem. Soc.* **2017**, *139*, 11361.
[113] L. A. Stern, L. Feng, F. Song, X. Hu, *Energy Environ. Sci.* **2015**, *8*, 2347.
[114] M. B. Stevens, L. J. Enman, E. H. Korkus, J. Zaffran, C. D. M. Trang, J. Asbury, M. G. Kast, M. C. Toroker, S. W. Boettcher, *Nano Res.* **2019**, *12*, 2288.
[115] N. Han, F. Zhao, Y. Li, *J. Mater. Chem. A* **2015**, *3*, 16348.
[116] W. Chen, H. Wang, Y. Li, Y. Liu, J. Sun, S. Lee, J. S. Lee, Y. Cui, *ACS Cent. Sci.* **2015**, *1*, 244.
[117] J. Liu, J. Zhou, S. Liu, G. Chen, W. Wu, Y. Li, P. Jin, C. Xu, *Electrochim. Acta* **2020**, *356*, 136827.
[118] Y. Tang, Q. Liu, L. Dong, H. B. Wu, X. Y. Yu, *Appl Catal B* **2020**, *266*, 118627.
[119] B. M. Hunter, W. Hieringer, J. R. Winkler, H. B. Gray, A. M. Müller, *Energy Environ. Sci.* **2016**, *9*, 1734.
[120] X. Li, X. Hao, Z. Wang, A. Abudula, G. Guan, *J. Power Sources* **2017**, *347*, 193.
[121] M. Casas-Cabanas, J. Canales-Vázquez, J. Rodríguez-Carvajal, M. R. Palacín, *J. Am. Chem. Soc.* **2007**, *129*, 5840.
[122] L. Li, Y. Feng, Y. Li, W. Zhao, J. Shi, *Angew. Chem., Int. Ed.* **2009**, *48*, 5888.
[123] J. Pérez-Ramírez, S. Abelló, N. M. Van Der Pers, *Chem. Eur. J.* **2007**, *13*, 870.
[124] F. Song, X. Hu, *Nat. Commun.* **2014**, *5*, 4477.
[125] Y. Han, Z. H. Liu, Z. Yang, Z. Wang, X. Tang, T. Wang, L. Fan, K. Ooi, *Chem. Mater.* **2008**, *20*, 360.
[126] D. S. Hall, D. J. Lockwood, S. Poirier, C. Bock, B. R. MacDougall, *J. Phys. Chem. A* **2012**, *116*, 6771.
[127] S. Klaus, Y. Cai, M. W. Louie, L. Trotochaud, A. T. Bell, *J. Phys. Chem. C* **2015**, *119*, 7243.
[128] B. Sriram, J. N. Baby, S. F. Wang, R. R. Mathiara, M. Govindasamy, M. George, *ACS Sustainable Chem. Eng.* **2020**, *8*, 17772.
[129] L. Peng, N. Yang, Y. Yang, Q. Wang, X. Xie, D. Sun-Waterhouse, L. Shang, T. Zhang, G. I. N. Waterhouse, *Angew. Chem., Int. Ed.* **2021**, *60*, 24612.
[130] J. T. Kloprogge, D. Wharton, L. Hickey, R. L. Frost, *Am. Mineral.* **2002**, *87*, 623.
[131] O. Diaz-Morales, D. Ferrus-Suspedra, M. T. M. Koper, *Chem. Sci.* **2016**, *7*, 2639.
[132] H. Yin, L. Jiang, P. Liu, M. Al-Mamun, Y. Wang, Y. L. Zhong, H. Yang, D. Wang, Z. Tang, H. Zhao, *Nano Res.* **2018**, *11*, 3959.
[133] F. Song, M. M. Busch, B. Lassalle-Kaiser, C. S. Hsu, E. Petkucheva, M. Bensimon, H. M. Chen, C. Corminboeuf, X. Hu, *ACS Cent. Sci.* **2019**, *5*, 558.
[134] J. Chen, F. Zheng, S. J. Zhang, A. Fisher, Y. Zhou, Z. Wang, Y. Li, B. B. Xu, J. T. Li, S. G. Sun, *ACS Catal.* **2018**, *8*, 11342.
[135] B. H. Lim, E. H. Majlan, A. Tajuddin, T. Husaini, W. R. Wan Daud, N. A. Mohd Radzuan, M. A. Haque, *Chin. J. Chem. Eng.* **2021**, *33*, 1.
[136] R. Wang, K. Inoguchi, M. Ohashi, S. Someya, T. Munakata, M. Ishida, H. Ito, *Int. J. Hydrogen Energy* **2021**, *46*, 37757.
[137] T. Malkow, A. Pilenga, G. Tsotridis, G. De Marco, *EU Harmonised Polarisation Curve Test Method for Low-Temperature Water Electrolysis*, Publications Office of the European Union, Luxembourg **2018**.
[138] P. Lettenmeier, R. Wang, R. Abouatallah, S. Helmly, T. Morawietz, R. Hiesgen, S. Kolb, F. Burggraf, J. Kallo, A. S. Gago, K. A. Friedrich, *Electrochim. Acta* **2016**, *210*, 502.
[139] E. López-Fernández, J. Gil-Rostra, J. P. Espinós, A. R. González-Elipe, A. De Lucas Consuegra, F. Yubero, *ACS Catal.* **2020**, *10*, 6159.
[140] J. O. Majasan, F. Iacoviello, J. I. S. Cho, M. Maier, X. Lu, T. P. Neville, I. Dedigama, P. R. Shearing, D. J. L. Brett, *Int. J. Hydrogen Energy* **2019**, *44*, 19519.
[141] A. Thust, J. Barthel, K. Tillmann, *J. large-scale Res. Facil. JLSRF* **2016**, *2*, 3.
[142] A. Kovács, R. Schierholz, K. Tillmann, *J. large-scale Res. Facil. JLSRF* **2016**, *2*, A43.